Climate Dynamics (2024) 62:7851–7868
https://doi.org/10.1007/s00382-024-07310-2

Global drought changes and attribution under carbon neutrality scenario

Xiaoyun Su[1,3] · Gang Huang[1,2,3] · Lin Wang[4] · Ting Wang[5]

Received: 4 January 2024 / Accepted: 31 May 2024 / Published online: 26 June 2024

Abstract

As the carbon-neutral target has been set, it is of great importance to investigate and attribute dry-wet climate response for which CO_2 emission is increasing, decreasing, and remaining stable over time. Therefore, our study utilize data from five models of the CMIP6 to analyze the spatiotemporal variations and attribution of global drought as presented by the Standardized Precipitation Evapotranspiration Index (SPEI) during periods of CO_2 increasing by 1% per year, decreasing by 1% per year, and remaining stable. During the CO_2 ramp-up period, potential evapotranspiration (PET) increases faster than precipitation (P), causing a decrease in SPEI. Conversely, a faster PET decrease than P leads to increased SPEI during the CO_2 ramp-down period. Spatially, low and mid-latitudes exhibit opposite trends to high latitudes, with the most pronounced responses observed in the Amazon, southern Africa, and Australia. After CO_2 returns to pre-industrial (PI) concentration, global P and PET do not recover, remaining ~2% higher compared to PI levels. However, SPEI shows a recovery in the global average, yet fails to reach PI levels in specific regions. Furthermore, extreme drought and wetness events persist with increased frequency and severity compared to PI levels despite the recovery of CO_2 concentration. Finally, based on the attribution analysis, the contribution of precipitation (~35%) to drought changes is secondary to that of PET (~65%), which is primarily promoted by air temperature (~50%), followed by net radiation (~10%) and relative humidity (~6%) with negligible effect of wind speed.

Keywords Drought · Carbon neutrality · SPEI · CDRMIP · Attribution analysis

1 Introduction

Since the industrial revolution, anthropogenic activities have resulted in an extraordinary rise in the concentration of greenhouse gases (GHG), specifically carbon dioxide (CO_2), due to the extensive use of fossil fuels, deforestation, and other land use practices, contributing to global warming (Wang et al. 2021a) . Thus, acknowledging the urgency of the situation, member states of the United Nations Framework Convention on Climate Change (UNFCCC) adopted the Paris Agreement in December 2015, which aims to hold the increase in the global average temperature to below 2°C and to pursue efforts to limit the temperature increase to 1.5°C. Towards this target, atmospheric CO_2 concentration must peak and decrease continuously as soon as possible until carbon neutrality is achieved in this century (Sanderson et al. 2017; Rogelj et al. 2018; Wang et al. 2021a). However, it is important to note that the response of climate system to carbon neutrality remains inconsistent and inadequately comprehensive within the scientific community.

✉ Gang Huang
hg@mail.iap.ac.cn

✉ Ting Wang
wangting@mail.iap.ac.cn

[1] State Key Laboratory of Numerical Modeling for Atmospheric Sciences and Geophysical Fluid Dynamics, Institute of Atmospheric Physics, Chinese Academy of Sciences, Beijing 100029, China

[2] Laboratory for Regional Oceanography and Numerical Modeling, Qingdao National Laboratory for Marine Science and Technology, Qingdao 266237, China

[3] College of Earth and Planetary Sciences, University of Chinese Academy of Sciences, Beijing 100049, China

[4] Institute of Atmospheric Physics, CAS Key Laboratory of Regional Climate-Environment for Temperate East Asia, Chinese Academy of Sciences, Beijing 100029, China

[5] Carbon Neutrality Research Center, Institute of Atmospheric Physics, Chinese Academy of Sciences, Beijing 100029, China

Drought is considered as one of the most devastating natural disasters globally, often causing serious hazards to agriculture, ecosystems, and human communities (Huang et al. 2017a; Guan et al. 2019; UNCCD 2022). Under global warming, the drought conditions have unprecedentedly worsen in many parts of the world, especially those drought hotspots (regions that are frequently or severely impacted), such as the Mediterranean region, southern Australia, sub-Saharan Africa, and southern South America (Dai and Zhao 2017; Spinoni 2019; UNDRR 2021; Wang et al. 2024). In the future, under different representative concentration pathways (RCPs) or global warming levels (GWLs), global drought will become increasingly frequent and severe, with affected areas expanding especially under high emission scenarios, that is RCP 8.5 and GWL 4° (Huang et al. 2017b; Carrão et al. 2018; Spinoni et al. 2021; UNDRR 2021; Zhao and Dai 2021). On a regional scale, Spinoni et al. (2021) indicated that future drought will be more severe in Central America, Chile and southern Argentina, the Mediterranean region, the Atlantic region of Western Africa and southern Africa, southwestern China and the western and southern coastal areas of Australia. Similar spatial patterns can be obtained for hydrological drought (Prudhomme et al. 2014) and agricultural drought (Lu et al. 2019).

The increased frequency and severity of droughts due to global warming on the global and regional scale are widely recognized. However, as the carbon-neutral target has been set, it is of equal importance to investigate and attribute dry-wet climate response for which CO_2 concentration is increasing, decreasing, and remaining stable over time. To understand the response of climate system to carbon neutrality, the World Climate Research Programme (WCRP) started the Carbon Dioxide Removal Model Intercomparison Program (CDRMIP, Keller et al. 2018). It includes climate and carbon cycle reversibility experiment, where CO_2 is prescribed to increase at 1% per year to four times of preindustrial CO_2 and then decrease at 1% per year until again at a preindustrial level, after which the simulation continues for as long as possible. The scenario, climate responses, and dynamics of carbon neutrality will be significantly different from what we have experienced since the industrial revolution (Long et al. 2020; Hou et al. 2021; Huang et al. 2022a; Zhou et al. 2022). Based on the ideal experiment, extensive studies have been dedicated to the variations and dynamics of climate systems such as temperature, precipitation, sea level, and the Atlantic Meridional Overturning Circulation (AMOC) under carbon dioxide removal (CDR) (An et al. 2021; Yeh et al. 2021; Kim et al. 2022; Paik et al. 2023; Cao et al. 2023; Liu et al. 2023). However, although some studies have characterized regional or global drought changes through precipitation (Boucher et al. 2012; Zhang et al. 2023; Kim et al. 2023), direct analysis utilizing drought indices that comprehensively consider temperature, humidity, and other factors under carbon neutrality is still lacking.

Standardized Precipitation Evapotranspiration Index (SPEI) is a drought index that comprehensively considers multiple factors and characterizes drought at multi-scale. The SPEI can compare the drought severity through time and space since it can be calculated over a wide range of climates. It has a clear and understandable calculation process and can identify different drought types and impacts under global warming, thus it has been widely applied (Wang et al. 2014, 2021b; Spinoni 2019; Sun et al. 2019; Spinoni et al. 2020, 2021; Huang et al. 2022b). Among the numerous factors considered in the SPEI, temperature and precipitation are more significant. During the ideal CO_2 concentration change, the global mean surface temperature peaks several years after carbon removal is carried out because of inertia, and then decreases with the continuing carbon removal. The recovery process is slow due to the ocean's immense thermal inertia, and the global temperature does not return to pre-industrial (PI) level even if CO_2 does (Sun et al. 2021; Yeh et al. 2021). Following the peak CO_2 concentration, global and ocean precipitation continues to rise for several years, while changes in land precipitation are nearly symmetrical in response to varying CO_2 levels. The difference between ocean and land precipitation is attributed to the ocean's large heat capacity. Even after CO_2 recovery, the global mean precipitation and both ocean and land precipitation do not return back to their original state (Yeh et al. 2021). Additionally, in drought research, Boucher et al. (2012) revealed hysteresis response of drought characterized by soil moisture to CO_2 changes. Kim et al. (2023) identified hemispherically asymmetric arid area change defined by the Global Drought Index (GDI), which may cause by hemispherically asymmetric Hadley cell edge changes. Zhang et al. (2023) suggested symmetric CDR may result in a risk of local drought over the South Asian summer monsoon region.

In summary, to address the knowledge gap in considering multi-factor, multi-scale global drought analysis under CO_2 removal, we utilized the CDRMIP experiment within CMIP6. This experiment involves idealized simulations where CO_2 concentrations undergo a symmetric increase and decrease at a rate of 1% per year. This study examines the spatiotemporal changes and underlying drivers of global drought through SPEI, enabling a holistic understanding of drought patterns under carbon neutrality conditions. The introduction of data and methods is presented in Section 2. In Section 3, we present the changes in precipitation (P), potential evapotranspiration (PET), and the SPEI under carbon neutrality scenario. In Section 4, we carry out attribution analyses. Lastly, Section 5 provides the summary and discussion.

2 Data and methods

2.1 Data

The CDR-reversibility experiment of the CDRMIP is used in this study, which involves *piControl*, *1pctCO$_2$* and *1pctCO$_2$-cdr* simulations. The *1pctCO$_2$* experiment is derived from the Diagnostic, Evaluation, and Characterization of Klima (DECK) *piControl* experiment which is intended to reflect a nearly balanced state of the climate system under 1850 conditions. The *1pctCO$_2$* simulation starts from the 1850 state with an atmospheric CO_2 concentration of 284.7 ppm and gradually increases by 1% per year until it reaches four times that of the *piControl* simulation (1138.8 ppm; run for 140 years) (referred to as the ramp-up period). Then, it gradually decreases at the same rate back to the *piControl* level (referred to as the ramp-down period). After that, the CO_2 concentration should be kept at 284.7 ppm for as long as possible, but here only the subsequent 60 years are selected for analysis. Note that the only external imposed forcing is CO_2 concentration, while all other forcings are kept at 1850 levels (Fig. 1).

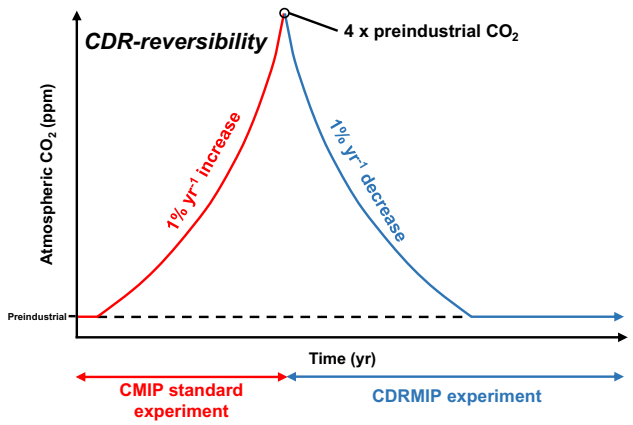

Fig. 1 Schematic diagram of the CDRMIP climate and carbon cycle reversibility experimental protocol (*CDR-reversibility*). From a preindustrial run at steady state atmospheric CO_2 is prescribed to increase and then decrease over a ~ 280-year period, after which it is held constant for as long as computationally possible. Modified from Keller et al. (2018)

In this study, PET and SPEI are computed using model output data for monthly precipitation; mean, maximum, and minimum air temperature; relative humidity; upwelling shortwave and longwave radiation; downwelling shortwave and longwave radiation; as well as 2-m wind speed. So far, nine models have participated in CDR-reversibility experiment. However, only the following five models (Table 1) are chosen to analyze the hydroclimate and drought changes (Section 3): ACCESS-ESM1-5, CanESM5, CNRM-ESM2-1, GFDL-ESM4, and MIROC-ES2L, because the others lack the necessary variables for this study. Based on the Taylor diagram presented in Fig. S1, these five models could effectively reproduce the observed pattern, with the Multi-Model Ensemble (MME) mean significantly outperforming individual models. At the interannual scale (Fig. S1(a)), the spatial correlation coefficients for P and PET between the MME mean and observations are 0.91 and 0.97, respectively. Similarly, at the seasonal scale (Figs. S1(b-e)), the corresponding correlation coefficients exceed 0.88 and 0.91 for P and PET, respectively. Therefore, based on the model evaluation, we conclude that utilizing these five models can effectively assess the response of future global drought changes to CO_2 forcing pathways. Among the chosen five models, ACCESS-ESM1-5 did not output relative humidity and wind speed, so the other four models are used for attribution analysis (Section 4). All output monthly data of the above five models are interpolated onto 2° latitude ×2° longitude, and the results are highly consistent across different resolutions (e.g., 1°×1°, 3°×3°). In addition, the global land cover map V2.3 compiled by European Space Agency is utilized to eliminate ice caps and desert regions where the high frequency of zero precipitation and water balances could potentially induce remarkable inaccuracies in the SPEI calculations (Vicente-Serrano et al. 2015; Spinoni et al. 2021).

Table 1 Summary of 5 models from CMIP6 used in this study

Model	Modeling center	Resolution (lat×lon)
ACCESS-ESM1-5	The Australian Community Climate and Earth System Simulator, Australia	1.25°×1.875°
CanESM5	Canadian Centre for Climate Modelling and Analysis, Canada	~2.8°×2.8°
CNRM-ESM2-1	Centre National de Recherches Météorologiques, France	~1.4°×1.4°
GFDL-ESM4	NOAA Geophysical Fluid Dynamics Laboratory, USA	1°×1.25°
MIROC-ES2L	Atmosphere and Ocean Research Institute (The University of Tokyo), National Institute for Environmental Studies, and Japan Agency for Marine-Earth Science and Technology, Japan	~2.8°×2.8°

2.2 The standardized precipitation evapotranspiration index

It is widely acknowledged that drought has multi-scale characteristics, for the time scale of water shortage accumulation is extremely important (McKee et al. 1993; Vicente-Serrano et al. 2010; Hayes et al. 2011; Wang et al. 2023). SPEI, proposed by Vicente-Serrano et al. (2010), is constructed based on P and PET, which can measure the severity of drought at multiple time scales. In general, drought originates from precipitation deficiency, initially manifesting as meteorological drought, which is commonly represented by SPEI at 1 month. Subsequently, agricultural drought ensues due to insufficient soil moisture, typically represented by SPEI at 3 or 6 months. Low recharge from the soil to water features such as streams and lakes causes a delayed hydrological drought, usually represented by SPEI at 12 or 24 months (Vicente-Serrano et al. 2012). The appropriate timescale varies when examining different hydrological systems and regions, necessitating the use of multi-scale drought index to capture the drought changes. Moreover, it is also suitable for detecting, monitoring, and exploring the impact of global warming on drought conditions since it can comprehensively consider the atmospheric evaporative demand affecting drought conditions. A brief computation of SPEI is sketched as follows (Vicente-Serrano et al. 2010).

(1) The monthly PET is calculated using the Penman–Monteith methodology (Allen et al. 1994):

$$PET = \frac{0.408\Delta\left(R_n - G\right) + \gamma\frac{900}{T+273}U_2\left(e_a - e_d\right)}{\Delta + \gamma\left(1 + 0.34U_2\right)}, \quad (1)$$

where Δ is the slope of the saturated vapor pressure function of temperature in $kPa/°C$; R_n is the net radiation in $MJ/(m^2 \bullet d)$; G is the soil heat flux in $MJ/(m^2 \bullet d)$; γ is the psychrometric constant in $kPa/°C$; T is the mean surface temperature in °C; U_2 is the wind speed at 2m in m/s; and e_a and e_d are the saturated and actual vapor pressure in kPa, respectively.

(2) The calculation of the difference between P and PET for month i is performed:

$$D_i = P_i - PET_i, \quad (2)$$

then the calculated Di values are aggregated at different time scales as follows, where n is the calculated month and k is the chosen time scale,

$$D_n^k = \sum_{i=0}^{k-1}\left(P_{n-i} - PET_{n-i}\right), n \geq k. \quad (3)$$

(3) The Log-logistic distribution is used to fit the probability distribution function of the D series:

$$F(x) = \left[1 + \left(\frac{\alpha}{x-\gamma}\right)^{\beta}\right]^{-1}, \quad (4)$$

where α, β, and γ are scale, shape, and origin parameters, respectively.

(4) The SPEI can be obtained as the standardized values of $F(x)$:

$$SPEI = W - \frac{C_0 + C_1 W + C_2 W^2}{1 + d_1 W + d_2 W^2 + d_3 W^3}, \quad (5)$$

where $W = \sqrt{-2\ln P}$, for $P \leq 0.5$, P being the probability of exceeding a determined D value, $P = 1 - F(x)$. When $P > 0.5$, P is replaced by $1 - P$ and the sign of the resultant SPEI is reversed. Furthermore, there are some constants: $C_0 = 2.515517$, $C_1 = 0.802853$, $C_2 = 0.010328$, $d_1 = 1.432788$, $d_2 = 0.189269$, and $d_3 = 0.001308$.

SPEI series are calculated in this work at time scales of 1, 3, 6, 12, and 24 months, but due to space constrains, only the results of 3 and 24 months are presented in the main text. The results of SPEI at other time scales are shown in the Supplementary Information.

2.3 EOF calculation

Empirical orthogonal function (EOF) analysis (Lorenz 1956) is among the most widely and extensively used methods in atmospheric science. The method, which decomposes a space-time field into spatial patterns and associated time indices, can extract the main features of the field. The brief calculation method is as follows.

First, process the annual gridded data into anomaly field $X_{m\times n}$, where m represents the number of grid points and n represents the number of years. Compute the covariance matrix $C_{m\times m}$ based on the matrix $X_{m\times n}$:

$$C_{m\times m} = \frac{1}{n} X_{m\times n} \bullet X_{m\times n}{}^{T}. \quad (6)$$

Then, calculate all eigenvalues $\lambda_1, \lambda_2, \ldots, \lambda_m$, and eigenvectors $V_{m\times m}$, ensuring that the condition is met:

$$C_{m\times m} \bullet V_{m\times m} = V_{m\times m} \bullet E_{m\times m}, \quad (7)$$

where $E_{m\times m}$ is a diagonal matrix containing eigenvalues:

$$E_{m\times m} = \begin{bmatrix} \lambda_1 & \cdots & 0 \\ \vdots & \ddots & \vdots \\ 0 & \cdots & \lambda_m \end{bmatrix}. \quad (8)$$

Arrange the eigenvalues in descending order: $\lambda_1 > \lambda_2 > \ldots > \lambda_m$. Then project the spatial modes onto matrix X to obtain the corresponding time coefficients:

$$PC_{m\times n} = V_{m\times m}{}^{T} \bullet X_{m\times n}. \tag{9}$$

Intuitively, the variance of matrix X can be reflected by the values of its eigenvalues, where higher λ indicate that the corresponding modes have a more significant proportion and contribute more to the total variance. The explained variance ratio of the *kth* mode to the total variance can be represented as:

$$R_k = \frac{\lambda_k}{\sum_{i=1}^{m} \lambda_i} \times 100\%, \tag{10}$$

Where R_k denotes the variance contribution of the *kth* mode. λ_i, λ_k denote the *ith* and *kth* eigenvalues, respectively, k=1, 2, …, p (p<m).

Finally, conduct statistical tests on the spatial modes, with the error range of the eigenvalues set to $\left[\lambda_i - \lambda_i\sqrt{\frac{2}{m}}, \lambda_i + \lambda_i\sqrt{\frac{2}{m}}\right]$. If the error ranges of adjacent modes do not overlap, the test is considered statistically significant; otherwise, it fails the significance test (North et al. 1982).

2.4 Attribution analysis

In this study, the contribution of P and PET to SPEI trend can be separated by a numerical experiment approach. According to the calculation procedure of PET above, the driving factors can be further decomposed into air temperature (Ta), net radiation (Rn), wind speed (U_2), relative humidity (Rh), and precipitation (P). Therefore, to determine the individual contributions of each factor to SPEI changes, six experiments have been designed, including one control experiment (*EXP_Ctr*) and five sensitivity experiments for each of above five driving factors (*EXP_Ta*, *EXP_Rn*, *EXP_U*$_2$, *EXP_Rh*, *EXP_P*). The control experiment is run with all original values during CO_2 concentration changes (years 1-280). In each sensitivity experiment, SPEI trend is re-calculated using one detrend input and four original inputs during the ramp-up (years 1-140, referred to as RU) and ramp-down (years 141-280, referred to as RD) periods, respectively (Table 2, Fig. S2).

In traditional way, the contribution of the *i*th factor to SPEI changes is represented as $C_i = V_{EXP_{Ctr}} - V_{EXP_i}$, where V_{EXP_Ctr} and V_{EXP_i} are the trends of the simulated SPEI in *EXP_Ctr* and *EXP_i*. However, this method may not accurately reflect the individual contributions of the driving factors due to the potential for interactions among these factors. In order to address the problem, Sun et al. (2014) proposed an improved method for separating the contribution of each factor:

Table 2 Numerical experiments design for attribution analysis

Experiments	Description
EXP_Ctr	Ta, Rn, U_2, Rh and P during 1-280
EXP_Ta	Detrended Ta, the others same as control test
EXP_Rn	Detrended Rn, the others same as control test
EXP_U$_2$	Detrended U_2, the others same as control test
EXP_Rh	Detrended Rh, the others same as control test
EXP_P	Detrended P, the others same as control test

$$\sum_{k\neq i}^{n} C_k = V_{EXP\_i}, \tag{11}$$

where $\sum_{k\neq i}^{n} C_k$ means the cumulative contributions of the driving factors except for *i*th factor to the SPEI trend; k is the sensitivity experiment for a given driving factor; and n is the number of sensitivity experiments (=5 here). By simultaneously solving multiple factors from Eq. (11), the contribution of one factor to the SPEI trend can be computed by:

$$C_i = \frac{\sum_{k\neq i}^{n} V_k - (n-2)V_i}{n-1}. \tag{12}$$

As reported by Sun et al. (2014, 2017), this new approach performed better than the traditional approach with higher accuracy and efficiency. In this study, the contributions of the five driving parameters (Ta, Rn, U_2, Rh, and P) are evaluated based on above method, and the joint contributions of Ta, Rn, U_2, and Rh can be regarded as the contributions of PET to SPEI changes.

To visually appreciate the magnitude of each factor's contribution, the relative contribution percentages can be calculated as follows. Since P and PET are the most directly related factors to SPEI, their relative contributions are presented by:

$$RC_i = \frac{|C_i|}{|C_P| + |C_{PET}|} \times 100\%, \tag{13}$$

where i is P or PET. After that, Ta, Rn, U_2, and Rh are variables directly related to PET, so we calculate their relative contributions to PET and then indirectly get which to SPEI:

$$RC_j = \frac{\left|C_j\right|}{\left|C_{Ta}\right| + \left|C_{Rn}\right| + \left|C_{U_2}\right| + \left|C_{Rh}\right|} \cdot RC_{PET} \times 100\%, \tag{14}$$

where j refers to Ta, Rn, U_2, or Rh.

3 Hydroclimate and drought changes under carbon neutrality scenario

Through the mathematical principle of the SPEI procedure, P and PET are two key climate variables determining the wet-dry condition. Therefore, the spatial and temporal patterns of long-term trends and seasonal signatures of P, PET, and SPEI in the changing CO_2 pathway are analyzed in this section, as well as the result of EOF analysis. In addition, we focus on the changes in extreme drought and wetness during different CO_2 phases.

3.1 Long-term trends

We first show the temporal evolution of continental mean P and PET in the CO_2 pathway relative to the *piControl* simulation (Figs. 2a and b). The values are plotted as the percentage change (%) relative to PI levels. In the CO_2 ramp-up period, P and PET both increase as atmospheric CO_2 rises. P reaches a peak of approximately 5.82% in the 145th year, and PET reaches a peak of approximately 19.81% in the 143rd year, which both lag a little bit behind CO_2 concentration peaks (the 140th year). In the CO_2 ramp-down period, as CO_2 concentration decreases, P and PET also quickly decrease. However, the decreasing rates (0.032%/yr for P and 0.131%/yr for PET) are slower (0.035%/yr for P and 0.146%/yr for PET) than the increasing rates. When CO_2 concentration returns to the PI level, P and PET remain approximately 1.43% and 2.82% above their initial values, respectively. Then, although P and PET continue to decline, neither P nor PET recovers to their PI state in the stable 60 years (1.16% for P and 2.17% for PET above PI levels).

In what follows, the composite effect of P and PET, and associated drought changes in terms of SPEI will be examined (Figs 2c and d). Although both P and PET increase during the CO_2 ramp-up period, it is evident that the increasing rate of PET exceeds that of P. Thus, according to the calculation principle of SPEI, decreasing tendency of SPEI and drier conditions are expected during the RU period. SPEI at time scales of 3 and 24 months both reach their lowest values in the 144th year with -0.50% and -0.84%, respectively. The faster rate of PET change than P is also observed during the RD period, which explains the increase in SPEI. After CO_2 concentration recovers to PI level, SPEI at all time scales keep increasing and almost recover to their initial values during stabilization period (Fig. S3).

Figure 3 shows the spatial distributions of the trend in P and PET during the RU and RD periods, and the uncertainty is quantified by the consistency of the sign. If at least four out of five models concur on the sign, the MME can be considered reliable. Most regions experience an increase in P during the RU period and a decrease during the RD period. However, the opposite trend is observed in Central America, the Amazon, the Mediterranean region, Southern Africa, and Australia, showing a decreasing trend followed by an increasing trend during the RU and RD period. In contrast to the change in P, PET shows a globally consistent increase/decrease as CO_2 concentration increases/decreases, with stronger signals in the Amazon, Southern Africa, and Australia.

The spatial patterns of the SPEI trends across different time scales are comparable, but the magnitudes of these trends differ (Fig. S4). At longer time scales, the changes in SPEI become more pronounced, reflecting the cumulative impact of drought and SPEI (Wang et al. 2014). Here we illustrate the spatial distributions of the trend in SPEI at time scales of 3 and 24 months as examples (Fig. 4). Overall, the global drought change seems to be dependent on latitude, with a drier trend in low and mid-latitudes during the RU period, whereas a wetter trend is observed in high latitudes (Spinoni et al. 2021). The changes during the RD period are opposite to those during the RU period. It is noteworthy that

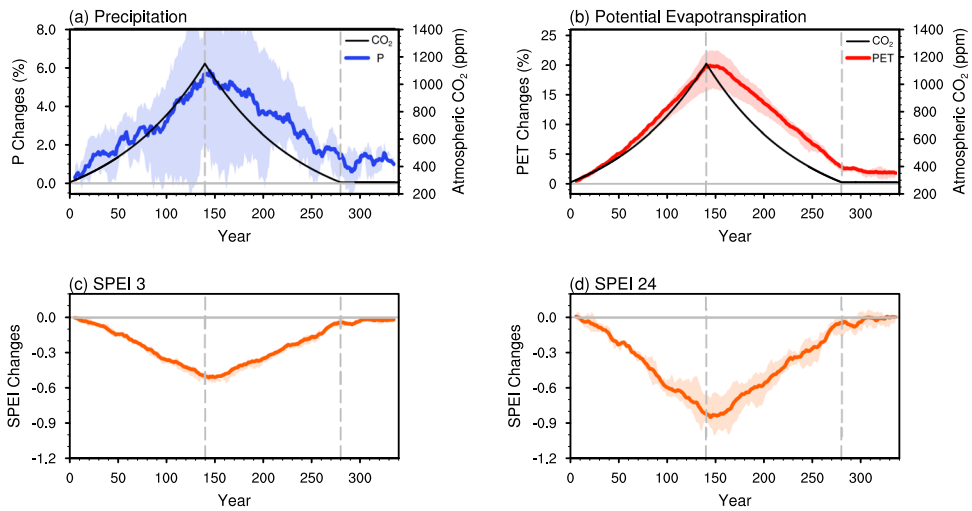

Fig. 2 Temporal changes of continental mean (**a**) precipitation, (**b**) potential evapotranspiration, and SPEI at time scales of (**c**) 3 and (**d**) 24 months during the CO_2 ramp-up, ramp-down, and stabilization periods relative to the PI levels. The black lines are the changes in CO_2 concentration. The colored lines and shadings denote the ensemble mean and interquartile range across five CMIP6 models, respectively

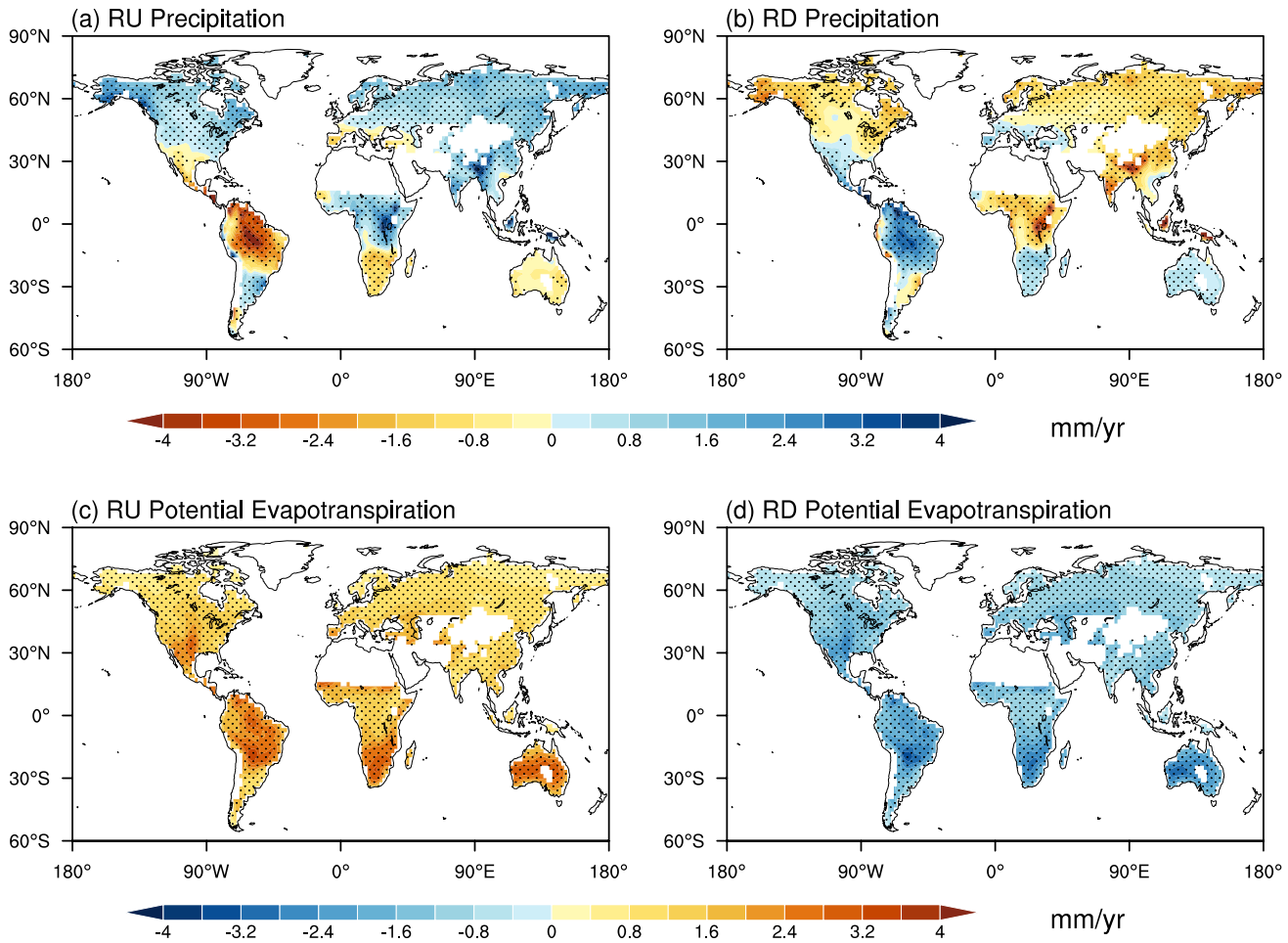

Fig. 3 Spatial distributions of the trend in (**a**, **b**) precipitation and (**c**, **d**) potential evapotranspiration during the CO_2 ramp-up and ramp-down periods. The stippling indicates that at least four out of five models agree on the sign of the MME

the changes are more pronounced and the models' behavior is more consistent in the Amazon, Southern Africa, and Australia due to the combined effects of decreasing/increasing P and increasing/decreasing PET during the RU/RD period (Fig. 3).

3.2 Seasonal signatures

To understand the change in each season, SPEI at the seasonal scale in May, August, November, and February are chosen to represent the drought in spring (March-May), summer (June-August), autumn (September-November), and winter (December-February) in the northern hemisphere, respectively. Similarly, the SPEI at the seasonal scale of November, February, May, and August are chosen to represent the drought in spring, summer, autumn, and winter in the southern hemisphere, respectively. The global mean changes for each season in a changing CO_2 pathway are shown in Fig. 5. The strongest changes are found in spring and summer, showing a decrease during the RU period and an increase during the RD period, with their minimum values being smaller than the annual minimum values (Fig. 2c). In winter, the trend is similar to that in spring and summer, but the magnitude is much smaller. Autumn exhibits the smallest spatial average dry-wet change compared to the other seasons. When CO_2 concentration returns to the PI level (the 280th year), SPEI fails to recover in all seasons except autumn. During the stabilization period, drought conditions could recover to PI levels in almost all seasons except spring.

Figure 6 displays the spatial distributions of the trend in four seasons during the RU and RD periods. The strongest change and the best model consistency (approximately 86% of the regions passed the consistency test) are observed in winter, with a noticeable trend of drying/wetting in regions south of 40°N during the RU/RD period, while the higher latitudes in the northern hemisphere experience the opposite. As a result, the global average variation in SPEI is relatively weak (Fig. 5). In summer, the SPEI trend is not strong in terms of spatial distribution (Figs. 6c and d), but the spatially averaged

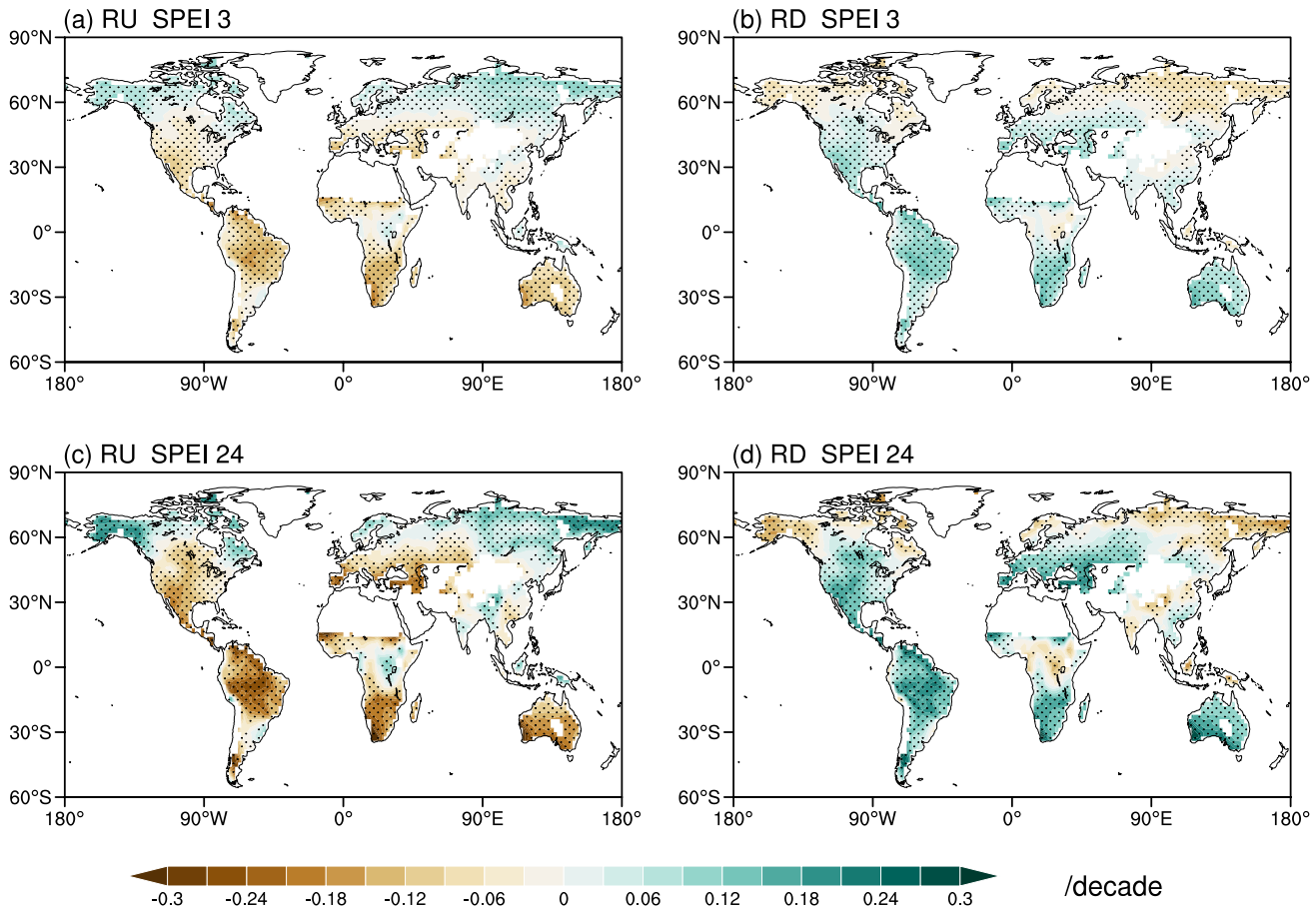

Fig. 4 The same as Fig. 3 but for SPEI at time scales of (**a**, **b**) 3 and (**c**, **d**) 24 months

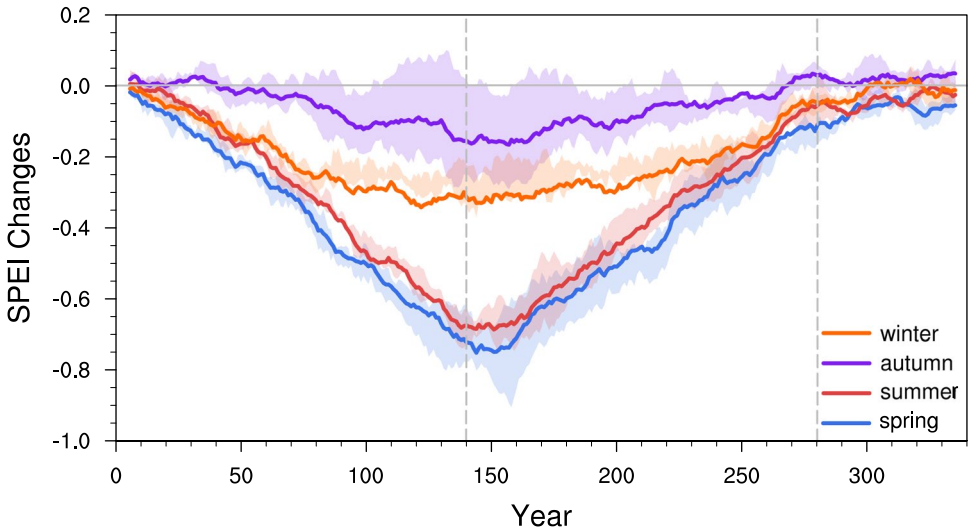

Fig. 5 Temporal changes of seasonal SPEI during the CO_2 ramp-up, ramp-down, and stabilization periods relative to the *piControl* simulation. The blue, red, purple, and orange lines indicate spring, summer, autumn, and winter changes, respectively, and the shading denotes the interquartile range across five CMIP5 models

change is instead more intense than winter because the global change is more consistent (Fig. 5), i.e., approximately 74% of the area becomes consistently drier/wetter during the RU/RD period.

3.3 EOF analysis

An EOF analysis is conducted on annual P, PET, and SPEI. The first mode of all variables demonstrates a significantly

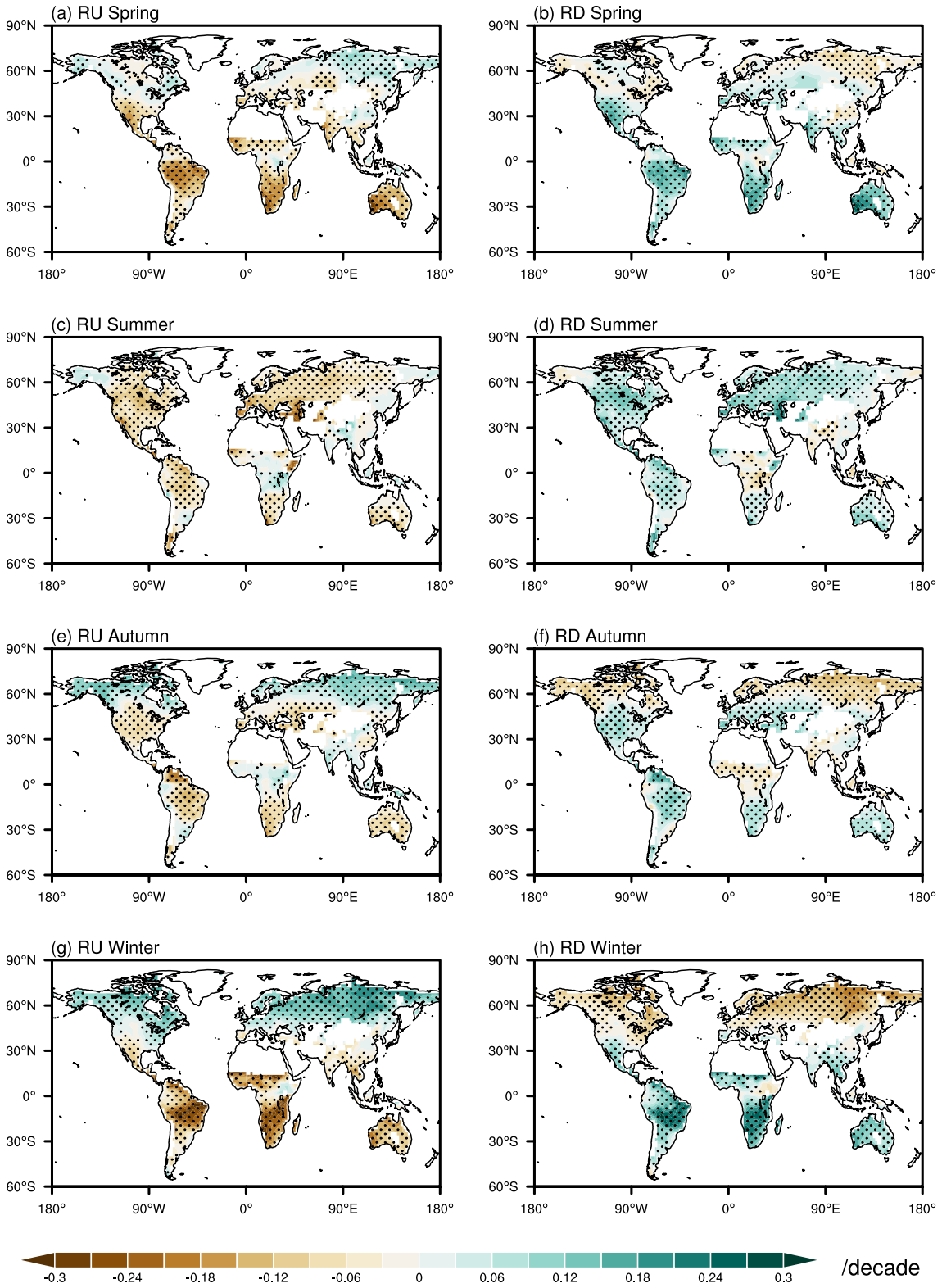

Fig. 6 Spatial distributions of the SPEI trend in (**a**, **b**) spring, (**c**, **d**) summer, (**e**, **f**) autumn, and (**g**, **h**) winter during the CO_2 ramp-up and ramp-down periods. The stippling indicates that at least four out of five models agree on the sign of the MME

higher variance contribution compared to other modes (Table 3). Additionally, all modes successfully passed the North test. Therefore, this section will primarily focus on the analysis of the first EOF mode (Fig. 7).

The first eigenvector (EOF1) loading pattern of precipitation explains 40.3% of the total variance (Fig. 7a), which is significantly higher than the second mode (5.4%). The EOF1 mode of P shows that the loading weights are not uniform, with Central America, the Amazon, the Mediterranean region, Southern Africa, and Australia exhibiting opposite signs from other places, and the strongest amplitude is near Amazon. According to the time series of the first principal component (PC1), there is a positive trend during the RU period while a negative trend during the RD period, indicating that P in the aforementioned regions is persistently decreasing during the RU period and increasing during the RD period, while the opposite trend is observed in other regions. The EOF1 loading pattern of PET explains 88.3% of the total variance (Fig. 7b), implying that the EOF1 mode could explain most of the PET changes. The EOF1 mode of PET shows that all the loading weights are positive, with stronger values generally located at 0-30°S in the southern hemisphere. According to the PC1, PET shows an increase followed by a decrease over all regions during the RU and RD period. It is worth noting that the anomalies of P and PET shown in EOF1 are strongest in the 147th and 144th year, respectively, both lagging slightly behind CO_2 concentration peak (the 140th year). During the CO_2 stabilization period, P and PET cannot return to their initial states.

The first EOF modes of SPEI at different time scales are quite similar (Fig. S5), so that here we only show SPEI at time scales of 3 and 24 months as examples (Fig. 7c and d). The first mode variance contributions of SPEI at different time scales are all above 55% (Table 3), which means their first modes could account for the majority of the SPEI changes. The EOF1 modes of SPEI at different time scales show negative loading weights mainly over low and mid-latitudes, whereas positive weights over high latitudes. According to the PC1, there is a positive trend during the RU period while a negative trend during the RD period, indicating that SPEI decreases over low and mid-latitudes (becoming drier) and increases over high latitudes (becoming wetter) during the RU period, and vice versa during the RD period. Note that the SPEI magnitudes at time scales of 3 and 24 months are strongest in the 147th and 148th year, respectively. During the CO_2 stabilization period, SPEI at different time scales do not return to their initial states.

3.4 Changes in extreme events

In the changing CO_2 pathway, not only the mean values but also extreme events should be concerned. Fig. 8 displays the probability distributions of SPEI in the five time periods at time scales of 3 and 24 months. The five time periods selected here are shown in Fig. 8a, which are the PI period (before atmospheric CO_2 changes, black shadow), 20 years of the CO_2 ramp-up period (years 56-75, blue shadow), 20 years around the CO_2 peak period (years 131-150, purple shadow), 20 years of the CO_2 ramp-down period (years 206-225, yellow shadow), and the CO_2 stabilization period (years 281-340, red shadow). The process of constructing probability distribution is as follows: for each model, values at all grids across the global land (excluding deserts and ice caps) for a specific period are extracted. These data from all models are then combined to create the probability distribution.

At all time scales, the distribution of SPEI during the PI period follows a standard normal distribution (Fig. S6), which is consistent with the mathematical principles used in the calculation of SPEI. During the RU period, the probability distributions of SPEI at all time scales become wider and their highest frequency decreases, indicating an increase in spatial variability and therefore, more frequent extreme events. Moreover, the mean values shift towards drought, with the central value of SPEI at the 24-month time scale decreasing from 0.0 during the PI period to -1.88 during CO_2 peak period, and the peak frequency decreasing from 8.46% to 3.98%. Meanwhile, the extreme drought (SPEI<-2) and extreme wetness (SPEI>2) occurrences greatly increase, with 25.68% and 14.52% increases for the SPEI at 24-month time scale, respectively. In particular, there is a noticeable increase in extreme drought in Central America, the Amazon, the Mediterranean region, South Africa, and Australia. Extreme wetness has increased notably in Alaska and the Chukchi Peninsula (Fig. S7). The SPEI probability distribution recovers as atmospheric CO_2 returns, but it remains wider than the distribution at the same CO_2 concentration during the RU period. Even when CO_2 completely recovers and remains stable, the probability distributions of SPEI at any time scale fail to return to PI conditions and become more extreme.

Table 3 The variation contributions of the EOF first three modes of precipitation, potential evapotranspiration, and SPEI at different time scales

Variables	P	PET	SPEI 1	SPEI3	SPEI 6	SPEI 12	SPEI 24
EOF1	40.3%	88.3%	67.7%	61.9%	56.6%	55.5%	62.3%
EOF2	5.4%	1.5%	2.5%	2.8%	3.4%	4.1%	4.2%
EOF3	2.8%	1.0%	2.2%	2.4%	2.6%	2.9%	2.2%

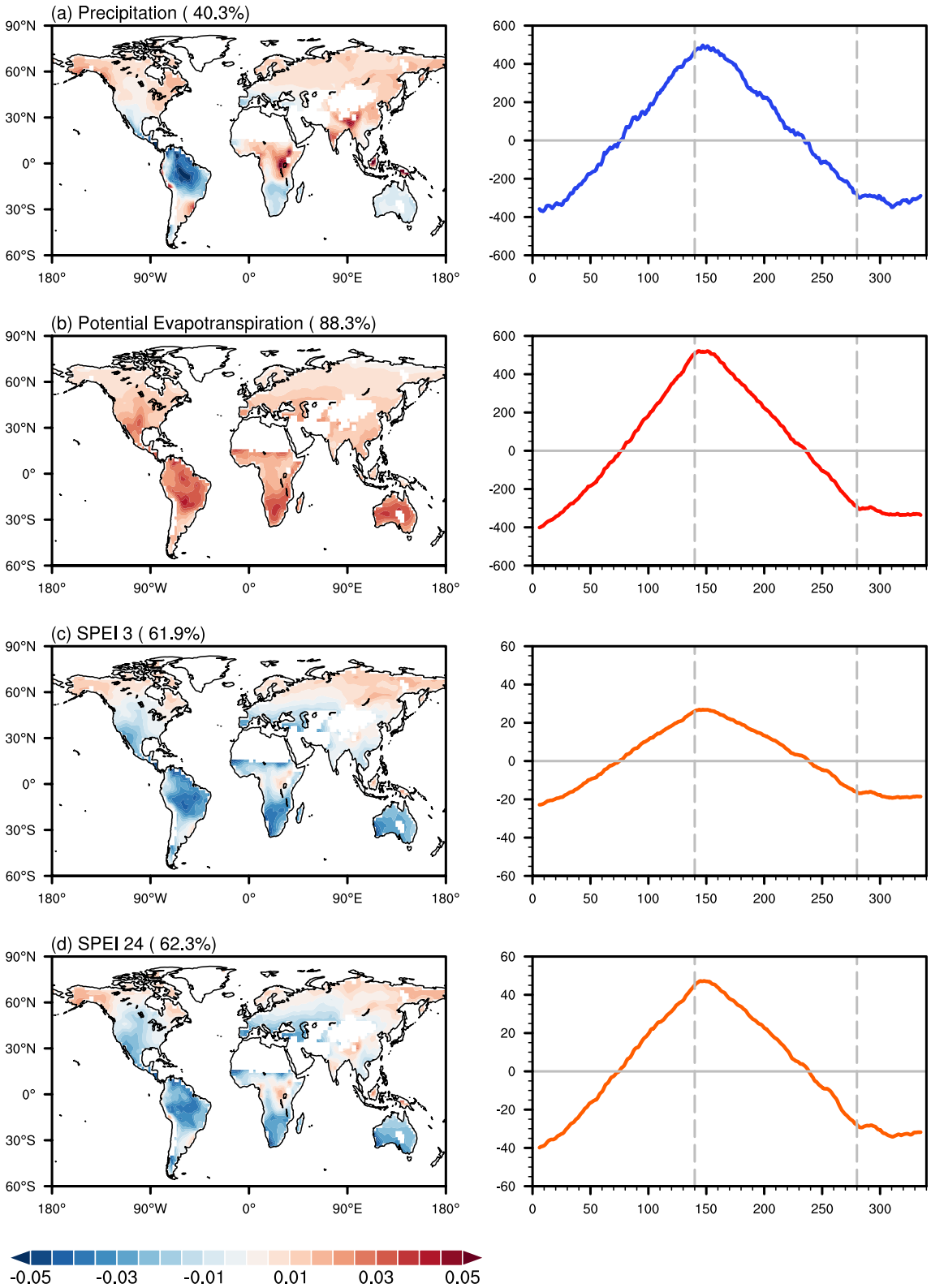

Fig. 7 The first EOF modes (left panels) and the corresponding time series of the principle component (right panels) of (**a**) precipitation, (**b**) potential evapotranspiration, and SPEI at time scales of (**c**) 3 and (**d**) 24 months

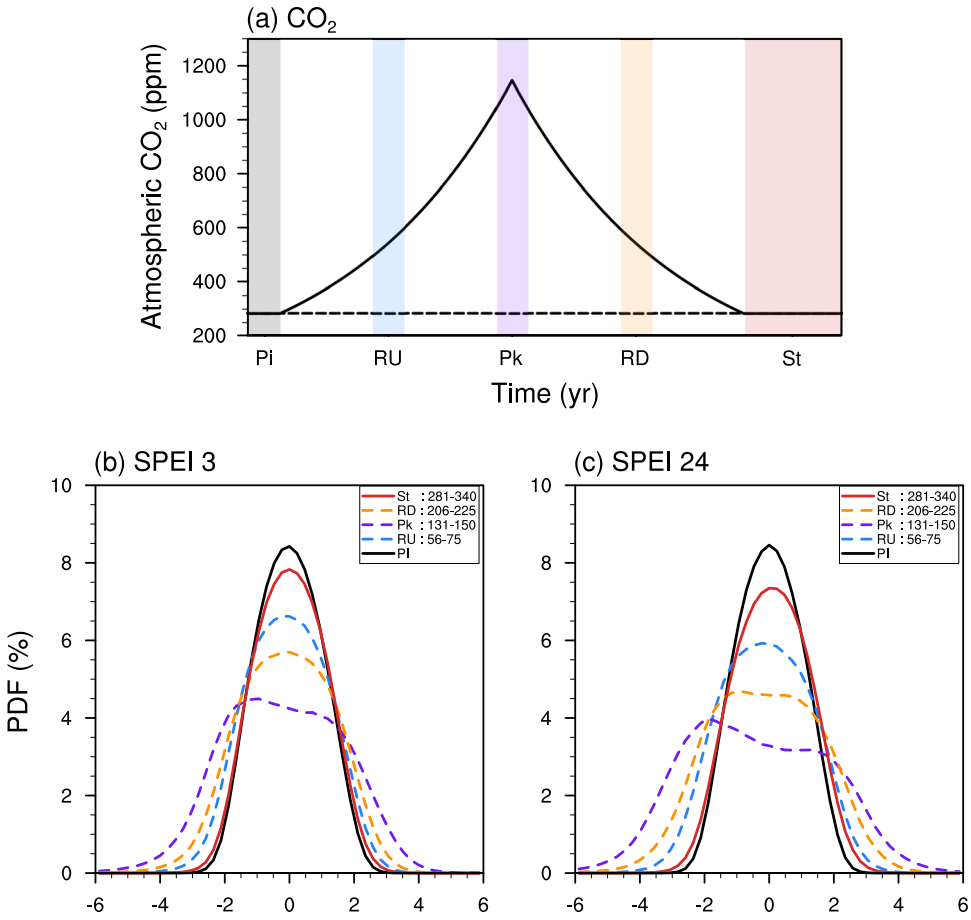

Fig. 8 **(a)** Evolution of atmospheric CO_2 concentration, and probability distributions of SPEI at the time scales of (**b**) 3 and (**c**) 24 months. The black, blue, purple, orange, and red lines and shadings represent the pre-industrial, CO_2 ramp-up, peak, ramp-down, and stabilization periods, respectively

4 Attribution of the drought changes under carbon neutrality scenario

According to SPEI procedure (Eqs. (1-5)), we attribute the SPEI changes to five factors: Ta, Rn, U_2, Rh, and P. The scatterplot that displays the accumulated contributions of each influence factor ($\sum_{i=1}^{6} C_k$) against the SPEI trend in *EXP_Ctr* (V_{EXP_Ctr}) is shown in Fig. 9. The result obtained by this method is close to the 1:1 line, indicating that this attribution method is effective.

Figure 10 shows the contributions of each factor to SPEI changes during the CO_2 ramp-up and ramp-down periods.

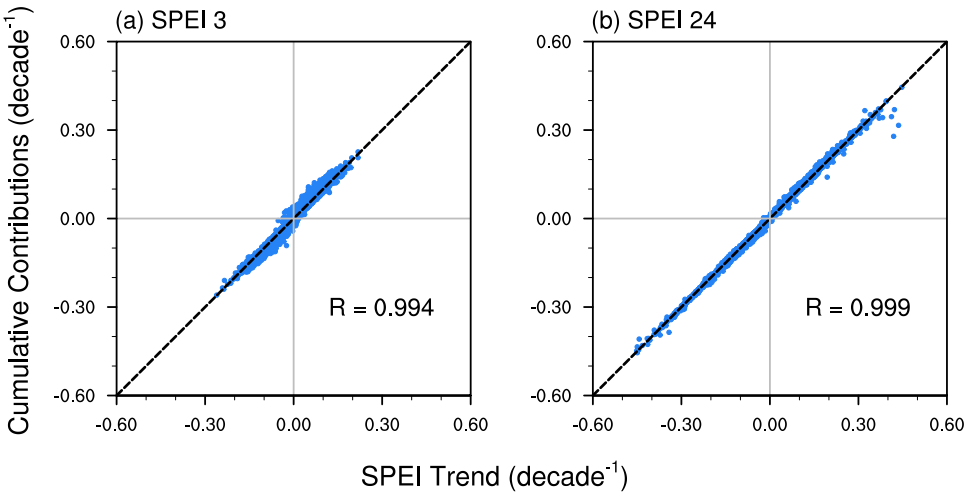

Fig. 9 Scatterplot of the accumulative contributions of each influence factor against the SPEI trend in *EXP_Ctr*

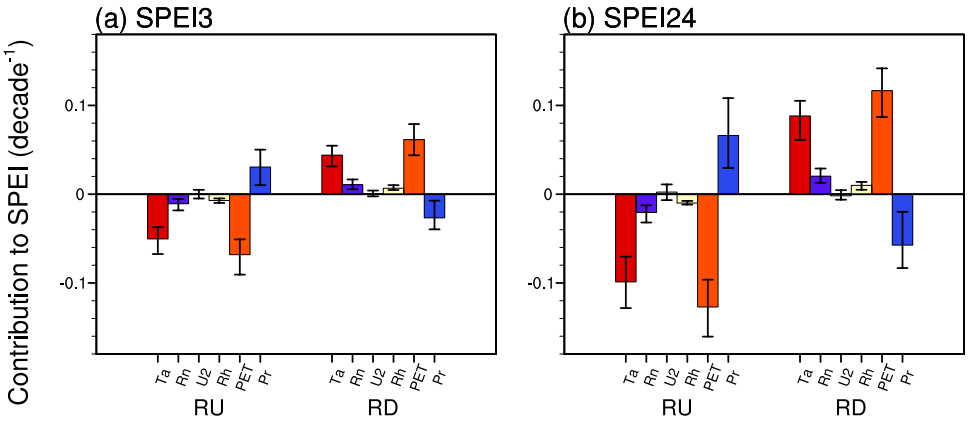

Fig. 10 Contributions of Ta, Rn, U_2, Rh, PET, and P to SPEI changes at time scales of (**a**) 3 and (**b**) 24 months during the CO_2 ramp-up and ramp-down periods (unit: decade^{-1}). Colored bars represent the ensemble mean, while the error bars denote the maximum and minimum values over four models

The contributions of each factor to SPEI changes at longer time scale are larger, for its greater changes (Fig. 2c and d), but their relative contributions to SPEI changes at different time scales are not significantly different. During the RU period, averaged P and PET both increase (Fig. 2a and b), but the relative contributions of P (31.00% to SPEI3, 34.23% to SPEI24) are smaller than those of PET (69.00% to SPEI3, 65.77% to SPEI24) (Table 4). In other words, the possible mitigation effect of increased precipitation may be completely outweighed by enhanced PET, resulting in decreasing SPEI and drying tendency. Similarly, during the RD period, the decrease in PET (69.75% to SPEI3, 67.01% to SPEI24) counteracts the decrease in P (30.25% to SPEI3, 32.99% to SPEI24), resulting in increasing SPEI and wetting tendency.

Subsequently, we decompose the contributions to PET into Ta, Rn, U_2, and Rh. We find that the main contributing factors are Ta and P, but they contribute to the SPEI changes with opposite signs. Among the other factors, Rn contributes the most (~10%), with a substantial dominance from longwave radiation over shortwave radiation (Table S1). The contributions from the other two factors, U_2 and Rh, are relatively insignificant. In conclusion, during the RU period, the increase in P is offset by the increase in PET which is primarily promoted by the increase in Ta and Rn, and the decrease in Rh (Fig. S8), resulting in decreasing SPEI and drying tendency. Similarly, during the RD period, the decrease in P is offset by the decrease in PET which is promoted by the decrease in Ta and Rn, together with the increase in Rh, resulting in increasing SPEI and wetting tendency.

In addition to the global mean, we then analyze the contributions of each factor to SPEI changes at pixel level for different time scales during the RU and RD periods (Figs. S9-16). The results are similar for different time scales except for their magnitude, and thus we illustrate the result of SPEI at the 3-month time scale as an example (Figs. 11 and 12). During the RU period, the contributions of Ta to SPEI changes are consistently negative around the world, and those of Rn are negative in a great majority of regions, while U_2 and Rh have both positive and negative contributions globally, which leads to small contributions when averaged globally (Fig. 10). Under the influence of these four factors, PET has contributed to lower SPEI (more negative). However, the contributions of P are not consistent globally, showing negative contributions to SPEI changes in Central America, Amazon, the Mediterranean region, Southern Africa, and Australia, and positive contributions in other regions, particularly stronger in the high latitudes. It is worth noting that both P and PET contribute to lower SPEI in the mentioned regions, making the decreases in SPEI especially noticeable over there (Fig. 4). As for high latitudes, the negative contributions of PET are partly counteracted by the positive contributions of P, resulting in a weaker increase in SPEI over there (Fig. 4). The spatial distributions of the contributions during the RD period are similar to those during the RU period, with opposite signs (Fig. 12), so the conclusions are similar and we do not repeat here.

In addition to the annual changes, we analyze the contributions to SPEI changes at seasonal scale (Fig. 13, Figs. S17-19, Table S2). The results reveal that the relative contribution of PET is highest in summer, exceeding 80%,

Table 4 Relative contribution of Ta, Rn, U_2, Rh PET, and P to SPEI changes at time scales of 3 and 24 months during the CO_2 ramp-up and ramp-down periods (unit: %)

		Ta	Rn	U_2	Rh	PET	P
SPEI3	RU	50.87	10.87	0.11	7.15	69.00	31.00
	RD	49.96	12.04	0.14	7.61	69.75	30.25
SPEI24	RU	49.30	10.30	1.19	4.99	65.77	34.23
	RD	49.13	11.32	1.02	5.54	67.01	32.99

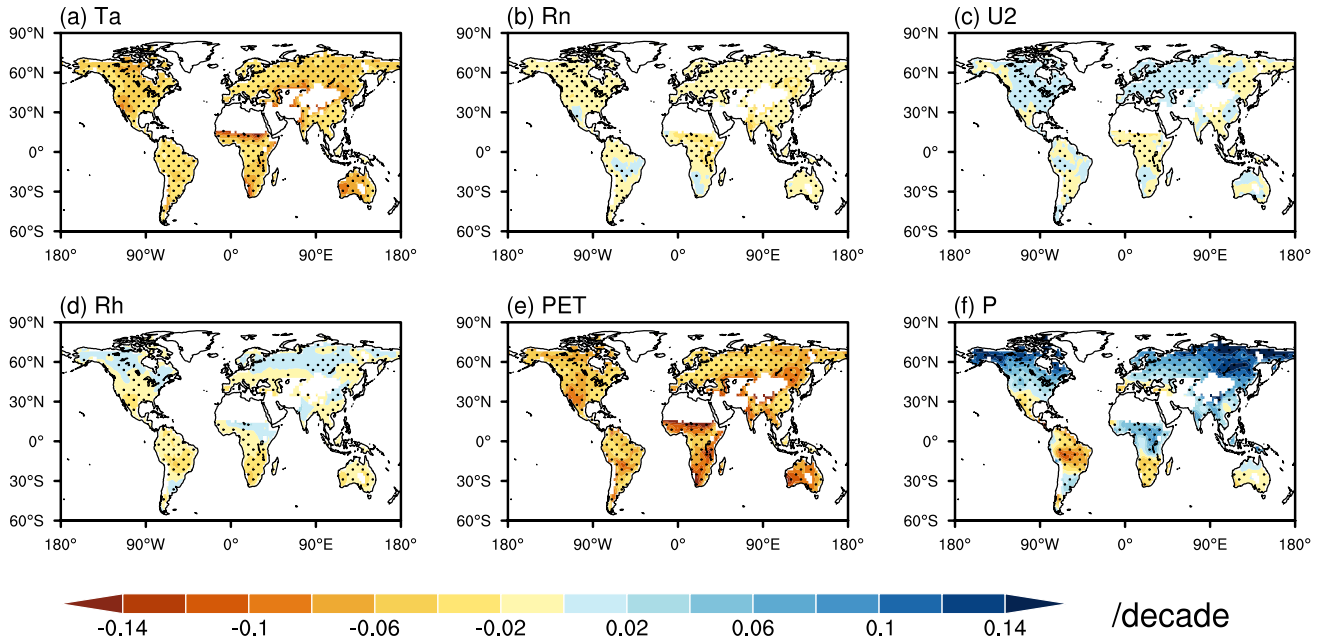

Fig. 11 Spatial distributions of the contributions of (**a**) Ta, (**b**) Rn, (**c**) U_2, (**d**) Rh, (**e**) PET, and (**f**) P to SPEI changes at time scale of 3 months during the CO_2 ramp-up period (unit: decade^{-1}). The stippling indicates that at least three out of four models agree on the sign of the MME

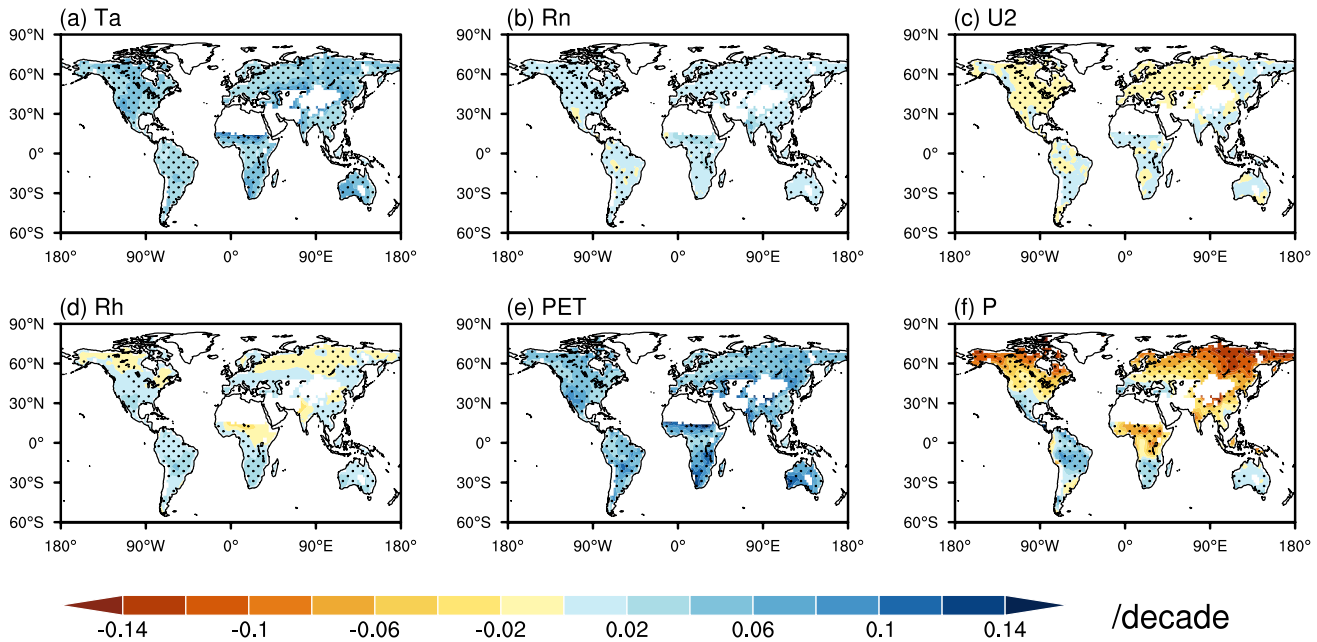

Fig. 12 The same as Fig. 11 but during the CO_2 ramp-down period

while P peaks in autumn, contributing of over 40% (Fig. 13, Table S2). In summer, the global dominance of PET (Fig. S17), which contributes notably more than P, leads to spatially consistent drier conditions during RU periods and wetter conditions during RD periods (Figs. S18-19). This results in consistent spatial dry-wet changes (Figs. 6a-d) and significant average trends (Fig. 5). However, due to the relatively small global average difference between PET and P contributions, which tend to offset each other, the global dry-wet change is weaker compared to summer (Fig. 5).

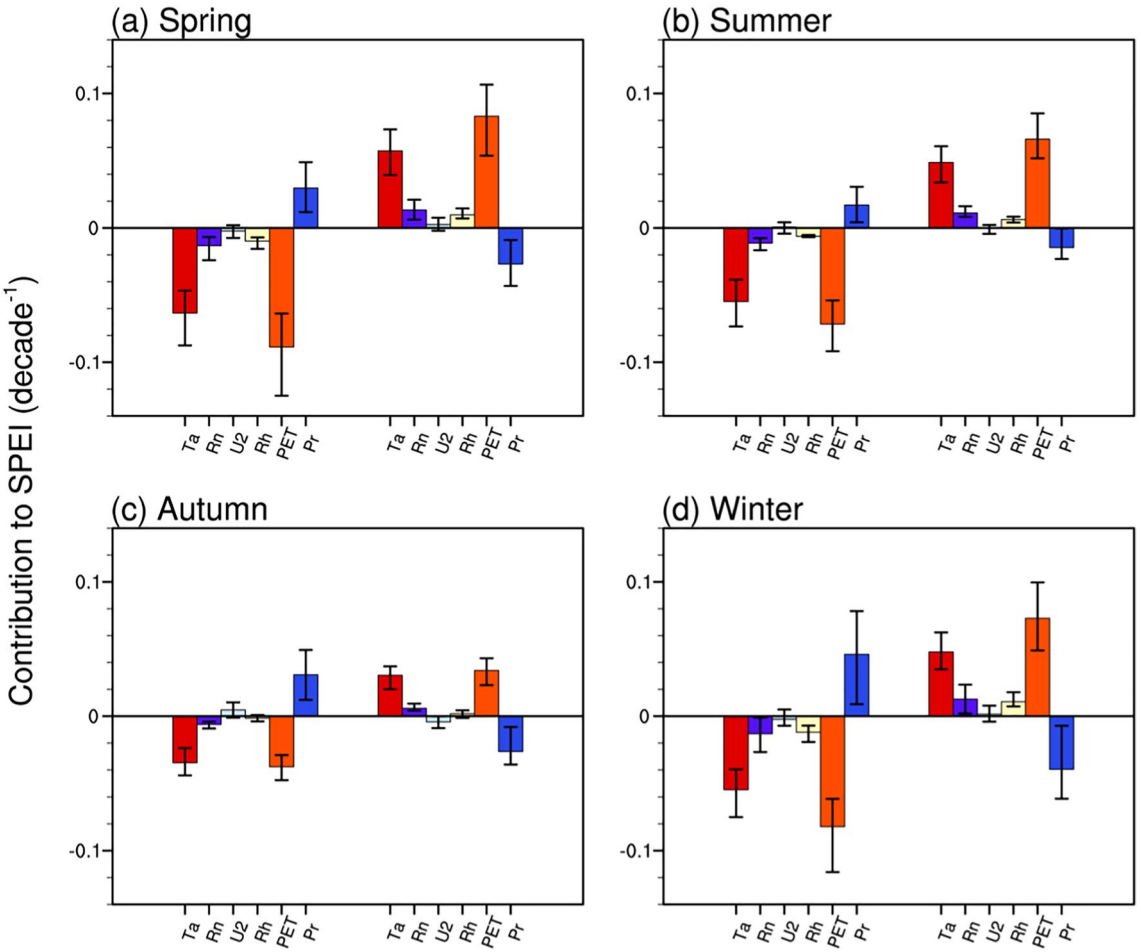

Fig. 13 The same as Fig. 10, but for (**a**) spring, (**b**) summer, (**c**) autumn, and (**d**) winter

5 Summary and discussion

By calculating the SPEI at different time scales which can characterize the dry and wet conditions based on five models of CMIP6, we analyze the spatial and temporal patterns of global dry and wet changes during CO_2 concentration increasing from its PI concentration (284.7 ppm) to four times of that (1138.8 ppm) at the speed of 1% per year, and then symmetrically decreasing at the same speed to PI level and keeping at 284.7 ppm for 60 years.

We preliminarily conclude that during the CO_2 ramp-up period, PET increases faster than P, causing the decrease in SPEI. Notably, changes in global P, PET, and SPEI lag behind the CO_2 concentration. Spatially, PET increases consistently, while P shows inconsistent changes globally. According to SPEI, low and mid-latitudes become drier, while high latitudes become wetter, with particularly severe dryness in the Amazon, Southern Africa, and Australia. During the CO_2 ramp-down period, PET decreases faster than P, causing an increase in SPEI. The spatial distributions are opposite to those during the RU period. After atmospheric CO_2 recovers to its PI level, P and PET do not fully recover in either global mean or spatial patterns. However, SPEI shows a recovery in the global average but fails to reach PI levels in specific regions. Seasonally, the globally averaged SPEI exhibits the strongest variation during spring and summer. However, the spatial distribution of SPEI is more pronounced in winter, showing drier/wetter in regions south of 40°N during the RU/RD period, while higher latitudes experience the opposite changes. In addition to the climatology, the changes in extreme drought (SPEI<-2) and wetness (SPEI>2) events are more concerning. As atmosphere CO_2 concentration increases, extreme events become more frequent and severe. Despite being relieved during the CO_2 stabilization period, the risk of extreme events is still higher than the PI level, indicating that extreme events including droughts and floods will become more common even though CO_2 recovers completely (Jo et al. 2022; Mondal et al. 2023).

Finally, we attribute SPEI changes to five factors: Ta, Rn, U_2, Rh, and P, and the joint contributions of the first four factors can be regarded as the contributions of PET to SPEI changes. In conclusion, during the RU period, the increase in P is offset by

the increase in PET, primarily promoted by the increase in Ta and Rn and the decrease in Rh, resulting in a decrease in SPEI and a drier world. Similarly, during the RD period, the decrease in P is offset by the decrease in PET, promoted by the decrease in Ta and Rn together with the increase in Rh, resulting in an increase in SPEI and a wetter world. In addition, the contribution of U_2 is too small to be discussed here.

Additionally, while we employ the traditional PM method for PET calculation, studies have shown that it does not account for the impact of atmospheric CO_2 changes on surface resistance, potentially overestimating PET and drought risks in future climates (Milly and Dunne 2016; Yang et al. 2019; Aadhar and Mishra 2020a, b). Therefore, we also utilize a modified PM method for drought estimation (Yang et al. 2019):

$$PET = \frac{0.408\Delta\left(R_n - G\right) + \gamma\frac{900}{T+273}U_2\left(e_a - e_d\right)}{\Delta + \gamma\left\{1 + U_2\left[2.4 \times 10^{-4}\left(\left[CO_2\right] - 300\right)\right]\right\}}, \quad (15)$$

where the terms are as defined in Eq. (1), but with an additional term accounting for an atmospheric $[CO_2]$ concentration effect. The recalculated results using this modified approach are presented in Figs. S20-23 and Table S3. Compared to the original PM method's results (Figs. 2, 3, 4, Fig. 10, and Table 4), the spatially averaged PET change is overestimated, leading to an overestimation of drought risk. Further attribution analysis reveals that the fertilization effect partially offsets the original drought trend and reduces the contribution of PET to SPEI changes from 65%-70% in the original PM method to 51%-56% in the modified method. However, our focus in this paper is not on quantifying the specific magnitude of drought risks, but rather on the trends and spatial patterns of changes. From this perspective, we find that both the overall direction and spatial patterns of changes remain consistent, regardless of whether the original or modified PM method is used for PET calculation.

SPEI is a meteorological drought index, and we also conducted a supplementary spatiotemporal analysis of soil moisture to corroborate the conclusions drawn from SPEI (Figs. S24-25). It can be seen that the global average soil moisture exhibited a similar behavior to the SPEI, characterized by a decrease during the CO_2 ramp-up period, indicative of a drier global condition, and a recovery during the CO_2 ramp-down period. However, since the infiltration of water into the soil requires some time (Boucher et al. 2012), the soil moisture reaches its lowest point about 50 years after the peak CO_2, reflecting a prolonged lag time compared to the SPEI. Meanwhile, it does not recover after CO_2 returns to PI level. In terms of spatial variations, during the CO_2 ramp-up period, there is noticeable drying in North America, the Amazon, southern Africa, Australia, and Russia. A wetting trend is noticed in these regions during the CO_2 ramp-down period, but it is less prominent compared to the drying trend. These results are basically consistent with SPEI-based findings, despite some differences in the magnitude.

Global warming not only intensifies the frequency of drought events but also disrupts their patterns, mechanisms, and impact processes, making them more irregular and complex. Some studies suggest that climate change has altered the global water cycle, disturbing the natural patterns of precipitation and evaporation, and leading to more frequent, prolonged, and severe droughts (Sheffield et al. 2012; Cook et al. 2020; Wu et al. 2022; Raposo et al. 2023). Drought generation and propagation are quite complicated, related to both local climate conditions and large-scale climate phenomena (e.g. El Niño Southern Oscillation—ENSO, Pacific Decadal Oscillation—PDO, Atlantic Multidecadal Oscillation—AMO and Arctic Oscillation—AO) (Dai 2011; Hao et al. 2017; Raposo et al. 2023). For instance, Funk et al. (2018) pointed out a connection between ENSO and droughts in southern Africa, with the 2015/2016 El Niño causing unprecedented drought in some catchment areas in the eastern portion of this continent. According to van Oldenborgh et al. (2021), during the 2019/20 bushfire in Australia, more than half of the July–December drought was driven by record excursions of the Indian Ocean Dipole and Southern Annular Mode. Furthermore, the combined effects of these large-scale phenomena can exacerbate global and regional droughts. According to Nguyen et al. (2021), when ENSO and PDO are in phase, many hotspots experience intensified and expanded droughts, particularly on longer timescales (6-12 months) . While research on drought has become quite extensive, the losses caused by drought disasters remain challenging to control and have profound impacts on agriculture, hydrology, and socioeconomic aspects. According to the report from UNCCD (2023), South Africa lost 33% of its grazing land due to drought; 85% of the population in middle- and low-income countries were affected by drought; 5 million people in southern China were affected by record-low water levels in the Yangtze River due to drought and prolonged heat; in 2022, Europe experienced a once-in-500-year extreme drought, with 630,000 square km^2 (roughly the combined area of Italy and Poland) affected by it; if global average temperatures rise 3°C above PI levels, an estimated 170 million people may experience extreme drought; if warming is limited to 1.5°C, 50 million fewer people will experience extreme drought. Consequently, achieving carbon neutrality is crucial to mitigate the impacts of global warming. However, carbon neutrality is a complex and comprehensive issue that goes beyond mere policy discussions and necessitates a scientific basis to inform decision-making. While the scenarios employed in this study may be idealized, and the MME result shown here could be model-dependent due to the small number of models (Hawkins and Sutton 2009; Xie et al. 2015), this study offers valuable insights for exploring and understanding the climate system's response to a carbon neutrality scenario.

Supplementary Information The online version contains supplementary material available at https://doi.org/10.1007/s00382-024-07310-2.

Acknowledgments We thank the editor and the two anonymous referees for their valuable comments that helped to improve the manuscript.

Funding This work was supported by the Second Tibetan Plateau Scientific Expedition and Research Program (2019QZKK0102), the National Natural Science Foundation of China Grants Nos. 42175041, 42141019, and 42261144687, the International Partnership Program of Chinese Academy of Sciences for Future Network (060GJHZ2022104FN), the Youth Program of the Institute of Atmospheric Physics, Chinese Academy of Sciences during the 14th Five-Year Plan period, and Key Deployment Project of Centre for Ocean Mega-Research of Science, Chinese Academy of Sciences (COMS2019Q03).

Data availability The CMIP6 outputs are available online at https://esgf-node.llnl.gov/search/cmip6/. The global land cover map V2.3 compiled by European Space Agency is download from http://due.esrin.esa.int/page_globcover.php.

Declarations

Competing interests The authors have not disclosed any competing interests.

References

Aadhar S, Mishra V (2020a) On the Projected Decline in Droughts Over South Asia in CMIP6 Multimodel Ensemble. J Geophys Res: Atmospheres 125 e2020JD033587. https://doi.org/10.1029/2020JD033587

Aadhar S, Mishra V (2020b) Increased Drought Risk in South Asia under Warming Climate: Implications of Uncertainty in Potential Evapotranspiration Estimates. J Hydrometeorol 21:2979–2996. https://doi.org/10.1175/JHM-D-19-0224.1

Allen R, Smith M, Pereira L, Perrier A (1994) An update for the calculation of reference evaporation. ICID Bull 43:35–93

An S-I, Shin J, Yeh S-W, et al (2021) Global Cooling Hiatus Driven by an AMOC Overshoot in a Carbon Dioxide Removal Scenario. Earth's Futur 9: e2021EF002165. https://doi.org/10.1029/2021EF002165

Boucher O, Halloran PR, Burke EJ et al (2012) Reversibility in an Earth System model in response to CO 2 concentration changes. Environ Res Lett 7:024013. https://doi.org/10.1088/1748-9326/7/2/024013

Cao L, Jin X-Y, Jiang J (2023) Simulated carbon cycle and Earth system response to atmospheric CO2 removal. Adv Clim Chang Res 14:313–321. https://doi.org/10.1016/j.accre.2023.03.001

Carrão H, Naumann G, Barbosa P (2018) Global projections of drought hazard in a warming climate: a prime for disaster risk management. Clim Dyn 50:2137–2155. https://doi.org/10.1007/s00382-017-3740-8

Cook BI, Mankin JS, Marvel K, et al (2020) Twenty-First Century Drought Projections in the CMIP6 Forcing Scenarios. Earth's Future 8: e2019EF001461. https://doi.org/10.1029/2019EF001461

Dai A (2011) Drought under global warming: a review. Wires Clim Change 2:45–65. https://doi.org/10.1002/wcc.81

Dai A, Zhao T (2017) Uncertainties in historical changes and future projections of drought. Part I: estimates of historical drought changes. Climatic Change 144:519–533. https://doi.org/10.1007/s10584-016-1705-2

de Raposo VMB, Costa VAF, Rodrigues AF (2023) A review of recent developments on drought characterization, propagation, and influential factors. Sci Total Environ 898:165550. https://doi.org/10.1016/j.scitotenv.2023.165550

Funk C, Harrison L, Shukla S et al (2018) Examining the role of unusually warm Indo-Pacific sea-surface temperatures in recent African droughts. Q J R Meteorol Soc 144:360–383. https://doi.org/10.1002/qj.3266

Guan X, Ma J, Huang J et al (2019) Impact of oceans on climate change in drylands. Sci China Earth Sci 62:891–908. https://doi.org/10.1007/s11430-018-9317-8

Hao Z, Yuan X, Xia Y et al (2017) An Overview of Drought Monitoring and Prediction Systems at Regional and Global Scales. Bull Am Meteorol Soc 98:1879–1896. https://doi.org/10.1175/BAMS-D-15-00149.1

Hawkins E, Sutton R (2009) The Potential to Narrow Uncertainty in Regional Climate Predictions. Bull Am Meteorol Soc 90:1095–1108. https://doi.org/10.1175/2009BAMS2607.1

Hayes M, Svoboda M, Wall N, Widhalm M (2011) The Lincoln Declaration on Drought Indices: Universal Meteorological Drought Index Recommended. Bull Am Meteorol Soc 92:485–488. https://doi.org/10.1175/2010BAMS3103.1

Hou H, Qu X, Huang G (2021) Reversal Asymmetry of Rainfall Change Over the Indian Ocean During the Radiative Forcing Increase and Stabilization. Earth's Futur 9:e2021EF002272. https://doi.org/10.1029/2021EF002272

Huang J, Li Y, Fu C et al (2017a) Dryland climate change: Recent progress and challenges: Dryland Climate Change. Rev Geophys 55:719–778. https://doi.org/10.1002/2016RG000550

Huang J, Yu H, Dai A et al (2017b) Drylands face potential threat under 2°C global warming target. Nat Clim Change 7:417–422. https://doi.org/10.1038/nclimate3275

Huang G, Xu Z, Qu X et al (2022a) Critical climate issues toward carbon neutrality targets. Fundamental Res 2:396–400. https://doi.org/10.1016/j.fmre.2022.02.011

Huang J, Mondal SK, Zhai J, et al (2022b) Intensity-area-duration-based drought analysis under 1.5°C–4.0°C warming using CMIP6 over a climate hotspot in South Asia. J Clean Prod 345: 131106. https://doi.org/10.1016/j.jclepro.2022.131106

Jo S-Y, Seong M-G, Min S-K, et al (2022) Hysteresis Behaviors in East Asian Extreme Precipitation Frequency to CO2 Pathway. Geophys Res Lett 49:e2022GL099814. https://doi.org/10.1029/2022GL099814

Keller DP, Lenton A, Scott V et al (2018) The Carbon Dioxide Removal Model Intercomparison Project (CDRMIP): rationale and experimental protocol for CMIP6. Geosci Model Dev 11:1133–1160. https://doi.org/10.5194/gmd-11-1133-2018

Kim S-K, Shin J, An S-I, et al (2022) Widespread irreversible changes in surface temperature and precipitation in response to CO2 forcing. Nat Clim Chang 1–7. https://doi.org/10.1038/s41558-022-01452-z

Kim S-Y, Choi Y-J, Son S-W, et al (2023) Hemispherically asymmetric Hadley cell response to CO2 removal. Sci Adv 9:eadg1801. https://doi.org/10.1126/sciadv.adg1801

Liu C, An S-I, Jin F-F, et al (2023) ENSO skewness hysteresis and associated changes in strong El Niño under a CO2 removal scenario npj Clim Atmos Sci 6 1–10. https://doi.org/10.1038/s41612-023-00448-6

Long S-M, Xie S-P, Du Y et al (2020) Effects of Ocean Slow Response under Low Warming Targets. J Clim 33:477–496. https://doi.org/10.1175/JCLI-D-19-0213.1

Lorenz EN (1956) Empirical orthogonal functions and statistical weather prediction. Technical report, Statistical Forecast Project Report 1, Dept. of Meteor., MIT, 1956. pp. 49

Lu J, Carbone GJ, Grego JM (2019) Uncertainty and hotspots in 21st century projections of agricultural drought from CMIP5 models. Sci Rep 9:1–12. https://doi.org/10.1038/s41598-019-41196-z

McKee TB, Doesken NJ, Kleist J (1993) The relationship of drought frequency and duration to time scales. Eighth Conference on Applied Climatology, pp. 179–184

Milly PCD, Dunne KA (2016) Potential evapotranspiration and continental drying. Nat Clim Change 6:946–949. https://doi.org/10.1038/nclimate3046

Mondal SK, An S-I, Min S-K et al (2023) Hysteresis and irreversibility of global extreme precipitation to anthropogenic CO2 emission. Weather Clim Extrem 40:100561. https://doi.org/10.1016/j.wace.2023.100561

Nguyen P-L, Min S-K, Kim Y-H (2021) Combined impacts of the El Niño-Southern Oscillation and Pacific Decadal Oscillation on global droughts assessed using the standardized precipitation evapotranspiration index. Int J Climatol 41:E1645–E1662. https://doi.org/10.1002/joc.6796

North GR, Bell TL, Cahalan RF, Moeng FJ (1982) Sampling Errors in the Estimation of Empirical Orthogonal Functions. Mon Weather Rev 110:699–706. https://doi.org/10.1175/1520-0493(1982)110%3c0699:SEITEO%3e2.0.CO;2

Paik S, An S-I, Min S-K, et al (2023) Hysteretic Behavior of Global to Regional Monsoon Area Under CO2 Ramp-Up and Ramp-Down. Earth's Futur 11:e2022EF003434. https://doi.org/10.1029/2022EF003434

Prudhomme C, Giuntoli I, Robinson EL et al (2014) Hydrological droughts in the 21st century, hotspots and uncertainties from a global multimodel ensemble experiment. Proc Natl Acad Sci USA 111:3262–3267. https://doi.org/10.1073/pnas.1222473110

Rogelj J, Popp A, Calvin KV et al (2018) Scenarios towards limiting global mean temperature increase below 1.5 °C. Nat Clim Change 8:325–332. https://doi.org/10.1038/s41558-018-0091-3

Sanderson BM, Xu Y, Tebaldi C et al (2017) Community climate simulations to assess avoided impacts in 1.5 and 2 °C futures. Earth Syst Dyn 8:827–847. https://doi.org/10.5194/esd-8-827-2017

Sheffield J, Wood EF, Roderick ML (2012) Little change in global drought over the past 60 years. Nat 491:435–438. https://doi.org/10.1038/nature11575

Spinoni J, Barbosa P, Bucchignani E et al (2020) Future Global Meteorological Drought Hot Spots: A Study Based on CORDEX Data. J Clim 33:3635–3661. https://doi.org/10.1175/JCLI-D-19-0084.1

Spinoni J, Barbosa P, Bucchignani E et al (2021) Global exposure of population and land-use to meteorological droughts under different warming levels and SSPs: A CORDEX-based study. Int J Climatol 41:6825–6853. https://doi.org/10.1002/joc.7302

Spinoni J (2019) A new global database of meteorological drought events from 1951 to 2016. J Hydrol 24. https://doi.org/10.1016/j.ejrh.2019.100593

Sun S, Chen H, Ju W et al (2014) On the attribution of the changing hydrological cycle in Poyang Lake Basin, China. J Hydrol 514:214–225. https://doi.org/10.1016/j.jhydrol.2014.04.013

Sun S, Chen H, Sun G et al (2017) Attributing the Changes in Reference Evapotranspiration in Southwestern China Using a New Separation Method. J Hydrometeorol 18:777–798. https://doi.org/10.1175/JHM-D-16-0118.1

Sun S, Li Q, Li J et al (2019) Revisiting the evolution of the 2009–2011 meteorological drought over Southwest China. J Hydrol 568:385–402. https://doi.org/10.1016/j.jhydrol.2018.10.071

Sun M-A, Sung HM, Kim J, et al (2021) Reversibility of the hydrological response in east asia from CO2-derived climate change based on CMIP6 simulation. Atmosphere 12. https://doi.org/10.3390/atmos12010072

UNCCD (2022) Drought in numbers. https://www.unccd.int/resources/publications/drought-numbers

UNCCD (2023) GLOBAL DROUGHT SNAPSHOT 2023 | The need for proactive action. https://www.unccd.int/resources/publications/global-drought-snapshot-2023-need-immediate-action

UNDRR (2021) Special report on drought 2021. https://www.undrr.org/publication/gar-special-report-drought-2021

van Oldenborgh GJ, Krikken F, Lewis S et al (2021) Attribution of the Australian bushfire risk to anthropogenic climate change. Nat Hazards Earth Sys Sci 21:941–960. https://doi.org/10.5194/nhess-21-941-2021

Vicente-Serrano SM, Beguería S, López-Moreno JI (2010) A Multiscalar Drought Index Sensitive to Global Warming: The Standardized Precipitation Evapotranspiration Index. J Clim 23:1696–1718. https://doi.org/10.1175/2009JCLI2909.1

Vicente-Serrano SM, Beguería S, Lorenzo-Lacruz J et al (2012) Performance of Drought Indices for Ecological, Agricultural, and Hydrological Applications. Earth Interact 16:1–27. https://doi.org/10.1175/2012EI000434.1

Vicente-Serrano SM, Van der Schrier G, Beguería S et al (2015) Contribution of precipitation and reference evapotranspiration to drought indices under different climates. J Hydrol 526:42–54. https://doi.org/10.1016/j.jhydrol.2014.11.025

Wang L, Chen W, Zhou W (2014) Assessment of future drought in Southwest China based on CMIP5 multimodel projections. Adv Atmos Sci 31:1035–1050. https://doi.org/10.1007/s00376-014-3223-3

Wang F, Harindintwali JD, Yuan Z et al (2021a) Technologies and perspectives for achieving carbon neutrality. The Innovation 2:100180. https://doi.org/10.1016/j.xinn.2021.100180

Wang L, Chen W, Fu Q, et al (2021b) Super droughts over East Asia since 1960 under the impacts of global warming and decadal variability. Int J Climatol n/a. https://doi.org/10.1002/joc.7483

Wang L, Huang G, Chen W, Wang T (2023) Super Drought under Global Warming: Concept, Monitoring Index, and Validation. Bull Am Meteorol Soc 104:E943–E969. https://doi.org/10.1175/BAMS-D-22-0182.1

Wang L, Chen W, Huang G, et al (2024) Characteristics of super drought in Southwest China and the associated compounding effect of multiscalar anomalies. Science China Earth Sciences 67. https://doi.org/10.1007/s11430-023-1341-4

Wu G, Chen J, Shi X, et al (2022) Impacts of Global Climate Warming on Meteorological and Hydrological Droughts and Their Propagations. Earth's Future 10: e2021EF002542. https://doi.org/10.1029/2021EF002542

Xie S-P, Deser C, Vecchi GA et al (2015) Towards predictive understanding of regional climate change. Nat Clim Change 5:921–930. https://doi.org/10.1038/nclimate2689

Yang Y, Roderick ML, Zhang S et al (2019) Hydrologic implications of vegetation response to elevated CO2 in climate projections. Nat Clim Change 9:44–48. https://doi.org/10.1038/s41558-018-0361-0

Yeh S-W, Song S-Y, Allan RP, et al (2021) Contrasting response of hydrological cycle over land and ocean to a changing CO2 pathway. npj Clim Atmospheric Sci 4. https://doi.org/10.1038/s41612-021-00206-6

Zhang S, Qu X, Huang G, Hu P (2023) Asymmetric response of South Asian summer monsoon rainfall in a carbon dioxide removal scenario. npj Clim Atmos Sci 6:10. https://doi.org/10.1038/s41612-023-00338-x

Zhao T, Dai A (2021) CMIP6 Model-projected Hydroclimatic and Drought Changes and Their Causes in the 21st Century. J Clim 35:897–921. https://doi.org/10.1175/JCLI-D-21-0442.1

Zhou S, Huang P, Xie S-P et al (2022) Varying contributions of fast and slow responses cause asymmetric tropical rainfall change between CO2 ramp-up and ramp-down. Sci Bull. https://doi.org/10.1016/j.scib.2022.07.010